Catalysis Today 454 (2025) 115289

Contents lists available at ScienceDirect

Catalysis Today

journal homepage: www.elsevier.com/locate/cattod

Influence of operating conditions on the kinetics of Iron-catalysed gasification of biocarbons with CO_2

D. Chaos-Hernández, N. Latorre, P. Tarifa, E. Romeo, A. Monzón *

Instituto de Nanociencia y Materiales de Aragón-INMA, CSIC-University of Zaragoza, Zaragoza, Spain

ARTICLE INFO

Keywords:
Biocarbon
Catalytic gasification
CO_2 capture
Kinetics
Fe
Deactivation

ABSTRACT

In this study, we investigated the catalytic gasification of cellulose-derived biocarbons (CDC) with CO_2 using Fe as the catalyst. Fe(%wt)/CDC samples were synthesized through controlled pyrolysis of cellulose impregnated with iron precursors and evaluated under varying reaction temperatures and CO_2 concentrations. Characterization by XRD, TGA, Raman, TEM, and N_2 adsorption revealed that the initial Fe loading in cellulose not only determines the final carbon content in each Fe(%wt)/CDC sample but also plays a crucial role in regulating the textural and structural properties of the resulting carbonaceous materials, as well as the Fe nanoparticle size distribution. Specifically, higher Fe loading led to a decrease in surface area, reduction of microporosity, an increase of pore diameter, and to larger average Fe nanoparticle sizes. During gasification, Fe nanoparticles were oxidized by CO_2, resulting in a decline in catalytic activity and ultimately limiting the complete gasification of the carbonaceous material by the end of the reaction. These opposing effects explain the varying behaviour observed in the Fe(%wt)/CDC samples studied. Analysis of the initial gasification rates indicated that both, the apparent reaction order with respect to CO_2 and the activation energy, increased with reaction temperature and CO_2 partial pressure (p_{CO_2}), respectively. These results were successfully interpreted using a Langmuir-Hinshelwood model, which accounts for the influence of CO_2 adsorption on the observed reaction rate. These findings underscore the potential of Fe(%wt)/CDC materials for CO_2 utilization and biomass valorisation, providing valuable insights for the development of efficient catalytic gasification processes.

1. Introduction

In the current context of climate change and increasing energy demands, it is imperative to develop technologies capable of capturing and transforming carbon dioxide (CO_2). The effective implementation of these CO_2 valorization technologies is essential to move towards more sustainable energy models. However, although the conversion of CO_2 into useful and versatile molecules is of vital importance, its high thermodynamic stability means that any valorization route requires considerable energy consumption [1]. Among the methods employed, the Boudouard reaction in which solid carbon (charcoal) reacts with CO_2 to produce carbon monoxide (CO) stands out as one of the simplest and is a direct route for the conversion of CO_2:

$$C + CO_2 \leftrightarrow 2\ CO;\ \Delta H_{r,298K} = 172.46\ \text{kJ/mol}$$

This highly endothermic reaction requires temperatures above 700 °C for spontaneous CO production and can utilize CO_2 from a variety of combustion plants, including off-gas/flue gas and syngas [2].

Therefore, research conducted on the use of residual biocarbons obtained through biomass pyrolysis, which do not show good properties as adsorbents or in other applications, it is presented as a good alternative for its gasification with CO_2 [3]. After the gasification, the biocarbon is completely converted (except for the mineral fraction) into gaseous fuel products. Hence, the production of a cleaner gaseous fuel and the almost complete conversion of the initial biomass make the process of gasification of residual biocarbon a very attractive way of fully converting biomass into energy [4,5]. The gasification of biomass-derived biocarbon, instead of direct gasification of the raw biomass, has the relevant advantages of lower tar formation, thus reducing the problems caused by tar deposition in the equipment, greater energy efficiency, which partly compensates for the energy needed for biocarbon production, and the ease and reduction of logistics costs for transport and grinding. The CO obtained can be used in multiple processes, such as carbonylation reagent in the synthesis of chemical products. In addition, it is useful for obtaining synthesis gas,

* Corresponding author.
E-mail address: amonzon@unizar.es (A. Monzón).

https://doi.org/10.1016/j.cattod.2025.115289
Received 16 December 2024; Received in revised form 10 March 2025; Accepted 19 March 2025
Available online 28 March 2025

which is of great interest to produce products such as methanol, or liquid fuels through Fischer-Tropsch synthesis.

One of the disadvantages of CO_2 gasification is its slow kinetics. This is why, catalytic gasification, specifically with transition metals such as iron, is one of the main routes used to improve the kinetics due to its efficiency, availability and low cost [6–8].

Iron species with almost unlimited availability have been used as promising catalysts to improve the Boudouard reaction rate. In that sense, Ohtsuka [9] determined that $Fe(NO_3)_3$ presents a good catalytic activity attributed to obtaining smaller crystals of the active iron phases formed during devolatilization and gasification. On the other hand, Qi [10]; studied how iron modification affects the structure of a carbon and its gasification reactivity. They observed changes in the pores of the carbon and an increase in the formation of amorphous carbon, being α-Fe the main chemical form of iron in the charcoal samples after pyrolysis. Recently, Xu [8], report the advantages of using iron as a catalytic agent due to its low cost and high availability. However, catalyst deactivation of Fe catalytic phases remains as a major problem in the gasification process.

Therefore, this work proposes a kinetic study of CO_2 catalytic gasification with Fe, of biocarbons derived from cellulose taken as a reference compound. One of the fundamental aspects to be able to develop this process is the in-depth knowledge of the effects of the incorporation of the metallic nanoparticles within the carbon structure and how it modifies the surface chemistry of the biocarbon, modifying its physicochemical properties. The final goal is to quantify the impact of the different operating variables, reaction temperature and gas-feed composition, on the rate of gasification and of Fe deactivation.

2. Methodology

2.1. Preparation of catalytic biocarbons (Fe/CDC)

The biocarbon used in this study was a cellulose-derived biocarbon (CDC), synthesized through controlled thermal decomposition in a reducing atmosphere. Additionally, samples of "catalytic biocarbon" (defined as Fe(%wt)/CDC) were prepared using the same thermal decomposition conditions but previously impregnating the cellulose with the active metal (Fe) at different weight percentages (0.1, 0.5, and 1.0 %, relative to the fresh cellulose weight), following a protocol previously described [11]. For the synthesis, the cellulose initially was dried at 80 °C for 12 hours in an inert atmosphere. Subsequently, incipient wetness impregnation of the active metal was carried out using $Fe(NO_3)_3{\cdot}9\ H_2O$ as the precursor salt. In the next stage, thermal decomposition was performed in a reducing atmosphere with a total flow of 300 mL/min (50 % H_2 / 50 % N_2). The heating rate used was 50 °C/min until reaching the synthesis temperature of 800 °C, which was maintained for 1 hour. Finally, the sample was cooled to room temperature in the same atmosphere and superficial passivation of the metallic phase was performed by introducing a flow of N_2 at 150 mL/min and CO_2 at 50 mL/min.

2.2. Characterization techniques

The metallic content and thermal behaviour of the catalytic biocarbons was evaluated through thermogravimetric analysis in an oxidizing atmosphere (TGA-Air). A TGA/STA 851e *Mettler Toledo* instrument was used and the mass flows were controlled by T508606C1 flow meters. The measurements were recorded using the STARe Software version 8.10, provided by the same supplier, which documented the obtained data. A sample amount between 2 and 6 mg was reached, with a heating rate of 10 °C/min until a maximum temperature of 900 °C, under a constant flow of 50 mL/min of synthetic air (21 % O_2 / 79 % N_2). Since the carbonaceous support burns in an oxidative atmosphere and does not show any final residues, the metal content of the samples was calculated based on the weight of the remaining ashes, assuming element in their oxidation state as Fe_3O_4.

X-ray diffraction (XRD) patterns of the materials fresh and after reaction were obtained using a D8 Advance diffractometer from *Bruker Española S.A.*, with CuKα radiation (45 kV, 40 mA) at a wavelength of λ= 0.15418 nm. The scanned angle range (2θ) was from 10 to 90°, with measurements taken every 0.013° and a duration of 48.19 s per measurement. The obtained data were analysed using the High Score Plus v3.0 software to determine the peak positions (2θ) and the full width at half maximum (*FWHM*) of each peak. The phase composition was identified using the *ICDD* database. The crystallite size of the metallic species was calculated using the Scherrer equation [12].

Transmission electron microscopy (TEM) micrographs of the biocarbon and catalytic biocarbons were recorded using an *FEI Tecnai T-20* microscope, operated at 200 kV, on a copper TEM grid, and particle size distributions and mean particle diameters of the metallic species were calculated. In all cases, particle size distributions were calculated with a number greater than or equal to 300 particles observed in the TEM images. The diameter of each particle was measured using Scope Photo 3.0 software. Finally, the corresponding histogram was obtained from the collected data using OriginPro 8 from OriginLab Corporation. Raman spectroscopy was used to evaluate the carbon structure of the fresh biocarbon and catalytic biocarbons. Spectra were acquired using a *WiTec Alpha300* confocal Raman microscope with a 532 nm laser excitation beam. Raman spectra were collected from three different points on each sample within the Raman shift range of 500–2500 cm^{-1} .

The textural properties of the samples were analysed through N_2 adsorption-desorption isotherms at 77 K using a Tristar 3000 from *Micromeritics Instrument Corp*. The surface area was calculated using the Brunauer-Emmett-Teller (BET) method. Additionally, the total pore volume and average pore diameter were obtained using the Horváth-Kawazoe method.

2.3. CO_2 gasification tests

The gasification tests with CO_2 were carried out in a thermogravimetric system MK2-M5, (CI Precision Ltd, UK). This high-precision thermobalance, operating at atmospheric pressure, records data on weight sample as a function of time and temperature, allowing a direct measurement of the reaction rate under isothermal or dynamic experiments. The numerical derivative of weight vs. time data allow to obtain the gasification rate, $r_G=dW_T/dt$, for a given set of operating conditions. Dynamic experiments were carried out from room temperature until 950 °C, using a heating rate of 5 °C/min and a flowrate of 300 mL/min (N_2/CO_2=66.7 %/33.3 %). These experiments allowed to determine the temperature of maximum gasification rate for each sample. On the other hand, for isothermal tests, a sample of 50 mg was placed in the thermobalance and the system was heated under a nitrogen atmosphere at a heating rate of 10 °C/min until the selected reaction temperature (700, 725, 750, and 800 °C). Once reached, a CO_2 flow was introduced for 1 hour with a total flow of 300 mL/min, with CO_2 ratios of 8.3 %, 16.6 %, and 33.3 % relative to N_2.

3. Results and discussion

3.1. Chemical-physical characterization of catalytic biocarbons

TGA-Air profiles show CDC and Fe(%wt)/CDC (named on %Fe over CDC) (see Figure S1). The results showed three reaction zones. A weight loss of 3 % was observed for CDC, Fe(1.2 %wt)/CDC and Fe(4.7 %wt)/CDC in the temperature range of T^a-350 °C (1st reaction zone), which is attributed to the dehydration of the CDC. In the case of Fe(10.4 %wt)/CDC, a weight gain was observed in this zone due to the oxidation of Fe ions supported on the CDC, more pronounced in this case due to the greater amount of Fe contained in this material (Table 1). In the 2nd reaction zone, within the temperature range of 350–600°C, the greatest weight loss occurred in all samples due to the combustion of the

Table 1
Fe content and average particle diameter of Fe nanoparticles.

Samples	*%Fe Cellulose*	*%Fe CDC*	*dp, nm (XRD)*	*dp, nm (TEM)*
Fe(1.2 %wt)/CDC	0.1	1.2	12.3	15.5 ± 7.3
Fe(4.7 %wt)/CDC	0.5	4.7	15.4	20.8 ± 11.3
Fe(10.4 %wt)/CDC	1	10.4	28.2	28.7 ± 22.6

carbonaceous supports. Finally, in the third reaction zone, from 600 to 900 °C, complete combustion of the CDC was observed, with no residual ash, while in the case of the catalysts, a slight weight variation was noted, attributable to the oxidation of Fe present in the catalysts.

Table 1 compares the initial Fe contents, based on the initial amount of cellulose, with the final content obtained from the TGA-Air analyses. As expected, an increase in the final Fe content on the CDC compared to the initial theoretical amount can be observed, which is attributed to the formation of organic vapours and liquids that are removed during the thermal decomposition of cellulose.

Fig. 1 shows the XRD results obtained for the cellulose-derived biocarbon (CDC) samples and the Fe(%wt)/CDC catalytic biocarbons. In the case of the CDC, diffraction peaks corresponding to the carbon pattern forming the carbonaceous material are observed, with two very broad peaks at a 2θ angle of 24° and 44° (Ref. Code: 01–081–9116) [13,14]. On the other hand, the diffractograms of the Fe(%wt)/CDC materials show a crystalline structure with peaks associated with the diffraction pattern of metallic iron, with characteristic peaks at 26° and 43° attributed to carbon with a certain degree of graphitization (Ref. Code: 00–026–1077) and peaks attributed to Fe in 2θ value at 44° (Ref. Code: 01–071–4648). In the case of Fe(10.4 %wt)/CDC, which has a higher iron content, additional peaks appear at 65° and 82°. The patterns corresponding to the metallic species are identified in the form of metallic iron, and no peaks associated with its oxidized state are observed [6].

Additionally, the diffraction spectra obtained for the Fe(%wt)/CDC catalytic biocarbons show that as the amount of iron in the solid increases, the predominant diffraction peak intensifies and becomes sharper, indicating an increase in Fe crystallite size. The crystallite size, calculated from Scherrer equation, shows values of 12.3, 15.4 and 28.2 nm for the catalytic biocarbons with iron contents of 1.2, 4.7, and 10.4 %, respectively (Table1).

The structure of the catalytic biocarbons was also analysed using transmission electron microscopy. Fig. 2 shows the TEM images and the average particle size of the iron particles for the synthesized samples. CDC exhibits a smooth surface typical of carbonaceous materials. In the case of catalytic biocarbons, an increase in surface roughness is observed with the addition of iron. The metal is well dispersed over the carbonaceous material and bimodal particle size distributions are observed in all cases. As the amount of Fe in the sample increases, the particle size distribution is broader for Fe(1.2 %wt)/CDC, which are observed in a range of ~9–19 nm and ~28 nm, for Fe(4.7 %wt)/CDC of ~9–28 nm and ~38 nm, and in the case of Fe(10.4 %wt)/CDC of ~9–29 nm and ~63–67 nm, with the particle diameter distribution always being greater than 85 % for the smallest range in each material. Consequently, the average particle diameter also increases, being 15.46 nm for Fe (1.2 %wt)/CDC, 20.84 nm for Fe(4.7 %wt)/CDC and 28.71 nm for Fe (10.4 %wt)/CDC (Table 1). These results can be compared with the crystallite sizes obtained using the Scherrer equation applied to the XRD spectra, corroborating an increase in crystallite size with increasing Fe percentage in the sample.

The Raman spectra obtained for CDC and the prepared catalytic biocarbons show similarities between them, characteristics of materials based on carbonaceous compounds [15]. These materials are characterized by the clear presence of two peaks, one of them the D band, which is observed around 1350 cm^{-1} and indicates the number of defects present in the carbonaceous structure, and the second, known as the G band, which is observed around 1600 cm^{-1} and refers to the degree of graphitization of the carbonaceous material (Figure S2).

Using the intensities of the bands (I_D, I_G), information about the degree of disorder (I_G/I_D) can be obtained (Table 2). A decrease in the I_G/I_D ratio is observed when Fe is introduced in the sample, decreasing from 1.02 for CDC to 0.87 for Fe(10.4 %wt)/CDC. This fact indicates an increase in the number of defects present in the biomorphic carbon due to the addition of iron, as already mentioned in the TEM images. The disordered carbonaceous structure can help to improve the reactivity of gasification [16].

Finally, N_2 adsorption-desorption isotherms at 77 K were obtained from CDC and Fe(%wt)/CDC catalytic biocarbons, with the aim to evaluate the influence of the iron modification on the textural properties (see Fig. 3). Using the IUPAC classification [17], the isotherms obtained present a combination of Type II and Type IV, associated with materials with meso- and micro-porous solid characteristics. A low-pressure hysteresis caused by the lack of equilibrium can also be observed.

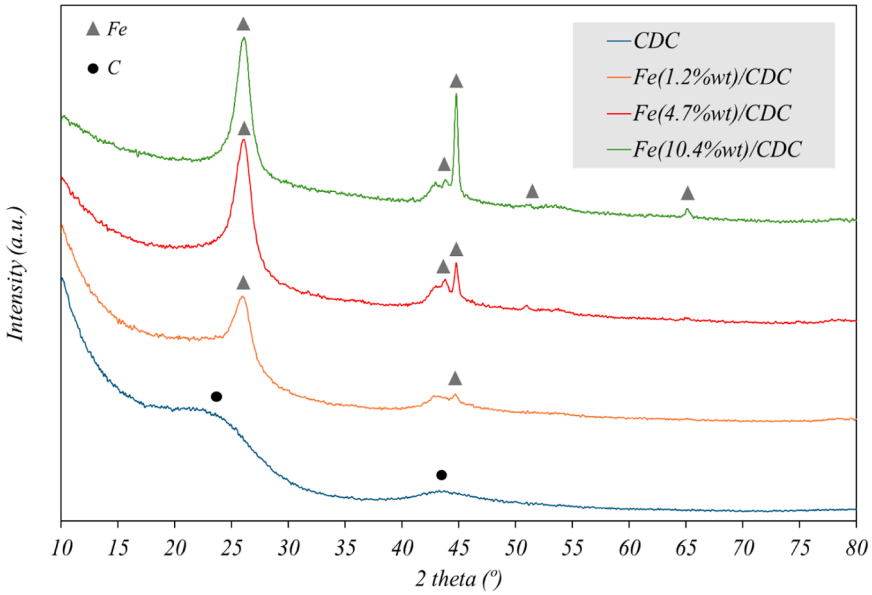

Fig. 1. XRD patterns of CDC and Fe(%wt)/CDC samples.

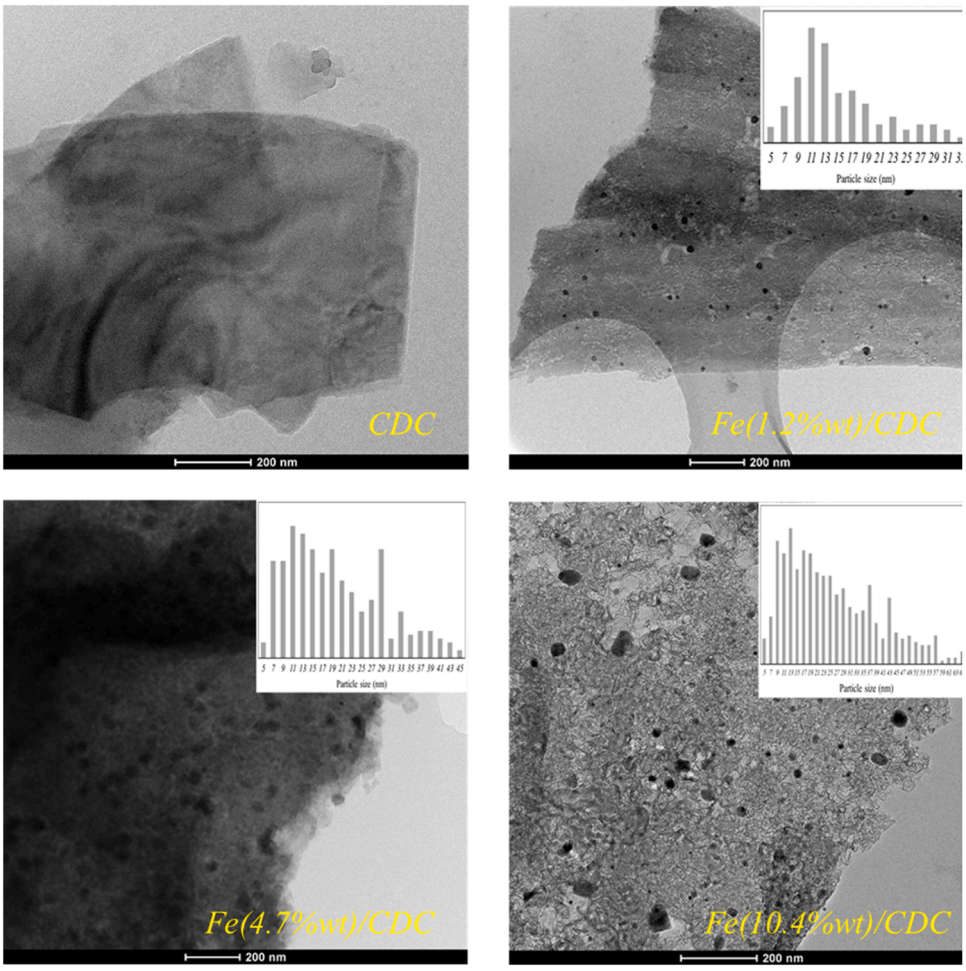

Fig. 2. TEM images of CDC and Fe(%wt)/CDC samples.

Table 2
Textural and structural properties of CDC and Fe(%wt)/CDC samples.

Samples	S_{BET} (m^2/g)	*Pore Volume* (cm^3/g)	*Pore Size* (Å)	*% μpore volume*	I_G/I_D
CDC	417	0.19	15.87	87	1.02
Fe(1.2 %wt)/CDC	452	0.29	24.43	53	0.92
Fe(4.7 %wt)/CDC	391	0.29	28.32	48	0.85
Fe(10.4 % wt)/CDC	267	0.24	35.75	34	0.87

Table 2 shows a summary of the textural properties of CDC and catalytic biocarbons. After the modification process with the Fe metal salt and thermal decomposition, both the surface area and the pore volume decrease as the metal percentage on the cellulose increases, from 452 to 267 m^2/g and 0.29–0.24 cm^3/g for CDC and Fe(10.4 %wt)/CDC respectively. Similar results were obtained by Qi [10] with the increase of iron loading.

In the case of the pore size, the observed effect is the opposite, showing an increase from the CDC, with 15.87 Å, to 35.75 Å for Fe (10.4 %wt)/CDC. As a result, the percentage of micropores decreased from 86.7, 52.8, 47.6–33.7 % from CDC to Fe(10.4 %wt)/CDC as the metal percentage increases. As expected, the iron introduced into the sample also affects the biocarbon synthesis process, producing a greater decomposition of cellulose, which translates into larger pore sizes and lower percentage of microporosity of the obtained biocarbon. Furthermore, the presence of Fe in the material can decrease the total surface area by blocking the micropores. These changes in the textural properties of the obtained catalytic biocarbons will affect the reactivity of CO_2 gasification, influencing factors such as the diffusivity of reactants and products throughout the reaction. In the work carried out by Koido [18], five types of carbons obtained from biomass were studied and the importance of pore size was highlighted, indicating that carbons with pore diameters < 24 Å are not suitable for CO_2 gasification applications because CO_2 cannot diffuse sufficiently into the pores.

3.2. Non-isothermal gasification tests

The results obtained from the weight sample measurements of CDC and Fe(%wt)/CDC catalytic biocarbons were plotted during non-isothermal gasification. Fig. 4 shows the values of sample mass (%) and reaction rate (DTG) during CDC and catalytic biocarbon gasification. As can be observed, the modification of the cellulose with iron improves the gasification process of the biocarbon formed, producing the diminution of the reaction temperature of the material. In the case of CDC, hardly any decrease in the weight of the material can be observed at 950 °C, confirming the high-energy requirement of the carbon gasification [14,18].

However, in the case of catalytic biocarbons, the materials are gasified with similar results at 750 °C. At the end of the experiment, all the samples are completely converted, reaching a final weight that corresponds to that of the Fe oxide, which depends on the amount of final Fe in the biocarbons (Table 1) and corroborates that at the end of the process the Fe remains in its oxidized state as Fe_3O_4.

The DTG curves confirm that the reaction rate increases as the

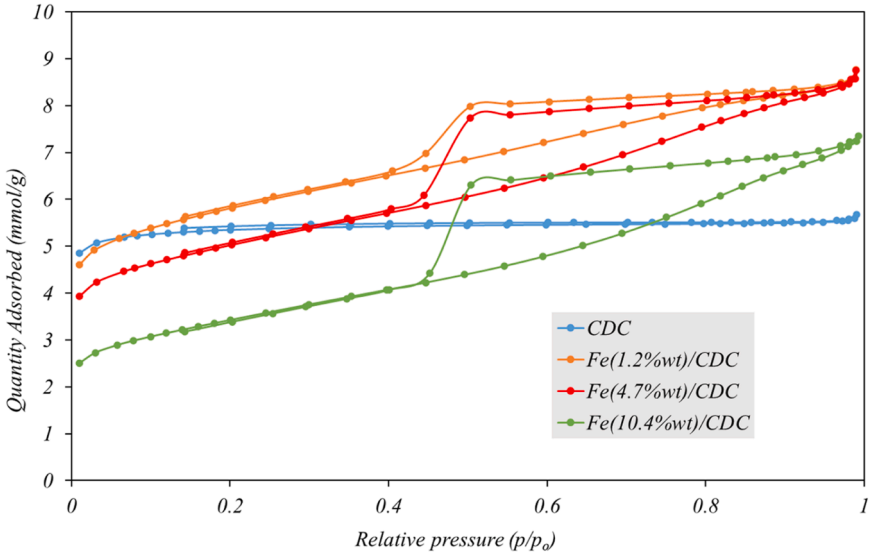

Fig. 3. N_2 adsorption isotherms of CDC and Fe(%wt)/CDC samples.

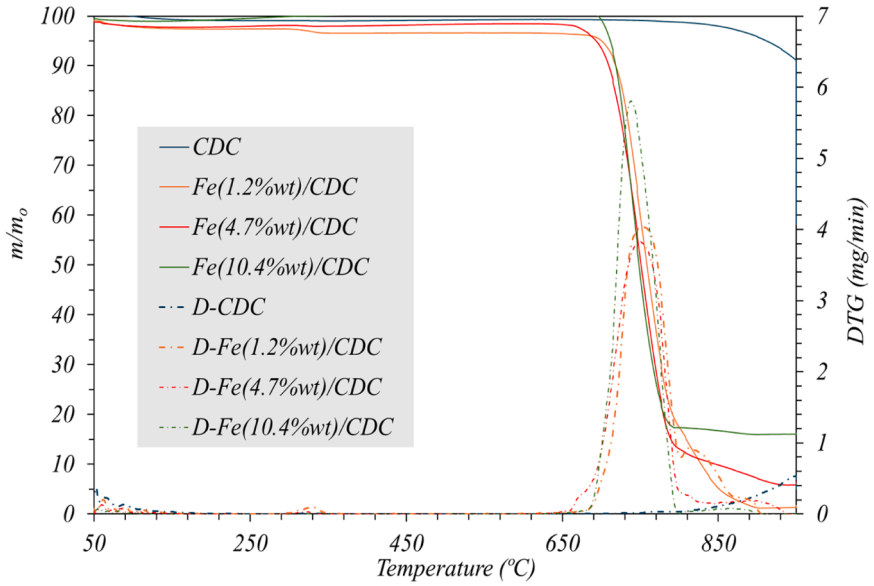

Fig. 4. TGA and DTG results from CDC and Fe(%wt)/CDC. Conditions: β= 5 °C/min, T_{end}= 950 °C, Q_{Total}: 300 mL/min, CO_2/N_2: 33.3 %/66.7 %.

percentage of iron in the biocarbon increases. Comparing the rates of the catalytic biocarbon, it can be seen that the reaction rate follows the following sequence: Fe(10.4 %wt)/CDC > Fe(4.7 %wt)/CDC > Fe (1.2 %wt)/CDC > CDC.

Another important factor that can influence the gasification process is the textural characteristics. In this case, as shown in Table 2, the increase in the amount of Fe increases the pore size of the biocarbon formed and decreases the percentage of microporosity and accordingly the volume of micropores, which facilitates the diffusion of both the reactants and the reaction products, thus enhancing de the gasification process.

In summary, the addition of Fe influences both the biocarbon formation process and its gasification. The higher percentage of Fe impregnated in the cellulose favours its gasification, increasing the number of defects and the average size of the pores created. These two factors, together with the higher percentage of metal, can also favour the CO_2 gasification of the biocarbon. On the other hand, high percentages of Fe diminish the surface area, leading to a higher particle size formed. Therefore, the best balance between these factors will produce the most effective catalytic biocarbon using the least amount of Fe possible. Analysing the results, regarding the temperature, rate and time required for the gasification of the biocarbon, the modification of the biocarbon with a percentage of iron of 1.2 and 4.7 % can be considered appropriate, achieving similar yields with lower quantities of necessary metal.

3.3. *Influence of operating conditions: reaction temperature and CO_2 concentration*

Fig. 5 show the influence of gasification temperature and CO_2 concentration on the evolution of mass of biocarbon (expressed as m/m_0) during gasification for the three Fe(%wt)/CDC samples. As regards the effect of temperature, their impact of the gasification rate, calculated from the slope of the curves in Fig. 5, depends on the Fe content and on the CO_2 concentration. Thus, for the sample with the lower Fe content, Fe(1.2 %wt)/CDC, the gasification rate presents an initial period of induction, characterized by a very low initial reaction rate. The duration

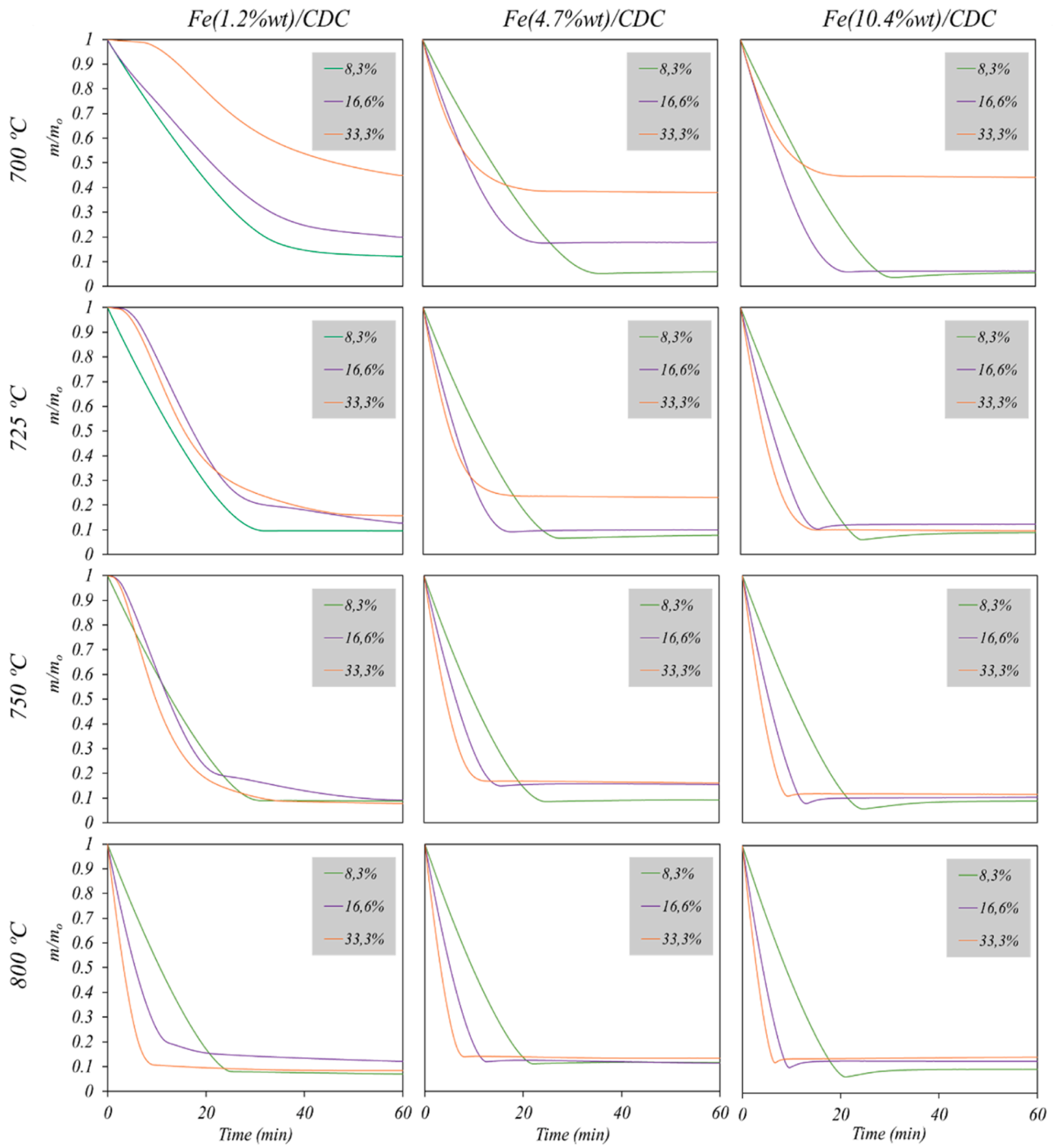

Fig. 5. Influence of CO_2 concentration and reaction temperature on mass decrease during gasification of Fe(%wt)/CDC samples.

of this is induction period decreases with the temperature but increases with the concentration of CO_2. However, for the samples with higher Fe loadings, 4.7 % and 10.4 %, this induction period is not observed, and the reaction rate decreases monotonically from the beginning of the reaction. The appearance on this zone of very low rate is consequence of the textural properties developed in the carbonaceous material during their synthesis. As it has been shown in Tables 1 and 2, the textural and structural properties of the carbonaceous material obtained, strongly depend on the Fe content used on the preparation of the sample. Thus, as the Fe loading decreases from 10.4 %wt to 1.2 %wt, the pore size decreases (from 3.6 nm to 2.4 nm) and the micropore volume (and their % with respect to the total pore volume) increases from 34 % to 53 %. In the case of CDC sample, the absence of Fe during their preparation produces a material with very low pore diameter (1.6 nm) and very high % of micropores (87 %). Therefore, the sample Fe(1.2 %wt)/CDC with low value of pore diameter will present severe restrictions to the internal diffusion of CO_2 through their porous structure and consequently very low reaction rate. As the reaction progresses, the pore diameter increases and diffusion restrictions decrease, with an observed increase in the reaction rate. These effects are clearly observed at temperatures below 750 ºC. At higher temperature, 800 ºC, the rapid gasification of the carbonaceous structure quickly opens the porous structure, and the diffusional restrictions are diminished accordingly. Diffusional restrictions are typically more severe at high reaction temperatures, as is the case in conventional catalysts where the support texture remains unaltered during the reaction. However, in this case, the rapid

gasification of the pore walls in the carbonaceous support, catalysed by the Fe nanoparticles dispersed within it, leads to a rapid increase in the effective pore diameter. This fact enhances CO_2 diffusion and substantially mitigates diffusion restrictions, even at high temperatures of gasification. For the other samples, Fe(4.7 %wt)/CDC and Fe(10.4 % wt)/CDC, the initial porous structure of the carbonaceous materials is sufficiently open, resulting in significantly lower diffusion restrictions for reactants and products from the onset of the reaction. In all cases, regardless of the CO_2 concentration, the gasification rate increases with temperature, as previously reported by Xie [13].

Interestingly, the duration of the induction period (see Fig. 5, sample Fe(1.2 %wt)/CDC) increases with CO_2 concentration, particularly at lower reaction temperatures. This behaviour is attributed to the activity loss of the Fe nanoparticles due to surface oxidation. As the CO_2 concentration rises, the deactivation rate accelerates, leading to a longer induction period. This rapid deactivation also results in incomplete carbon conversion by the end of the reaction, leaving a portion of the sample ungasified. This phenomenon is observed in all cases but is more pronounced at higher CO_2 concentrations. Additionally, the oxidation rate, and consequently the deactivation rate, increases with gasification temperature [15]. Thus, the complex temporal evolution of the gasification rates arises from the interplay of several competing factors, including CO_2 diffusion (determined by the initial texture of the carbonaceous material), the intrinsic reaction rate, and the oxidation/deactivation rate of the Fe nanoparticles. Both the reaction and deactivation rates are influenced by the reaction temperature and CO_2 concentration. These combined effects explain the crossing of the curves observed in Fig. 5, which is particularly evident for the Fe(4.7 % wt)/CDC sample with intermediate iron content.

Similar results were obtained by Micco [19], who studied the effect of CO_2 concentration (8–60 %) on the gasification of products derived from coal pyrolysis at 850 and 950 °C. Their results showed that at 850 °C, the reaction rate increased with a CO_2 concentration of 30 %. However, at 950 °C, the CO_2 concentration had no discernible effect on the reaction rate, suggesting a diminished sensitivity to the reagent at higher temperatures. Kibria [20] investigated coal gasification at higher temperatures (1000–1600 °C) and observed that increasing the CO_2 concentration accelerated the gasification rate, achieving complete carbon conversion more rapidly. Nevertheless, at elevated temperatures, the influence of CO_2 concentration on the gasification rate became negligible, indicating that the temperature dominates the process kinetics in this range. More recently, Ma [21] explored the effect of CO_2 concentration on gasification efficiency through gradient experiments (30 %, 50 %, 70 %, and 90 %). Their findings indicate that the CO_2 concentration significantly impacts gasification efficiency: reducing the CO_2 partial pressure decreases the maximum CO release rate but does not significantly alter the overall reaction rate. This behaviour was also attributed to incomplete gasification of the biocarbon under certain conditions. These results underscore the complex interplay between temperature, CO_2 concentration, and the nature of the carbon substrate and their impact on the gasification kinetics. The complete description and modelling of these coupled phenomena is being investigated and will be presented in a future work [22].

3.4. Characterization of catalytic biocarbons after gasification

In order to analyse the transformation of the metallic iron species after the gasification of the catalytic biocarbons with CO_2, XRD analyses were carried out for the Fe(%wt)/CDC catalytic biocarbons collected from the experiments carried out at 700 °C and 33.3 % CO_2 concentration (Fig. 6).

The results show the peak at 26º, corresponding to residual carbon, and the appearance of some peaks at 30°, 35°, 57°, 63° and 80°. These peaks are observed with greater intensity in the Fe(10.4 %wt)/CDC, which contains a higher percentage of iron prone to oxidation, and correspond to the metallic species in the form of Fe_3O_4, associated with its oxidized state (Ref. Code: 01–084–2782). Similar results were obtained by Nordgreen [23].

The crystallite sizes after gasification were calculated from the Scherrer equation, showing values of 46.8, 35 and 35.9 nm for the catalytic biocarbons with iron contents of 1.2, 4.7 and 10.4 %, respectively. This fact is related to the agglomeration of metallic species as the reaction progresses, which also produces the deactivation of the catalytic biocarbon.

This transformation of the metallic species was also observed by Zhang [6]. The authors studied the process at different gasification times, observing that the FeO peaks became increasingly more pronounced, while the metallic Fe peaks became less prominent, finally obtaining Fe_3O_4 in the coal sample after 2 h of gasification at 800 °C.

These results support the hypothesis made for the analysis of the results, which considers a competition between the gasification reaction of the biocarbon and the deactivation of the metallic phase of the

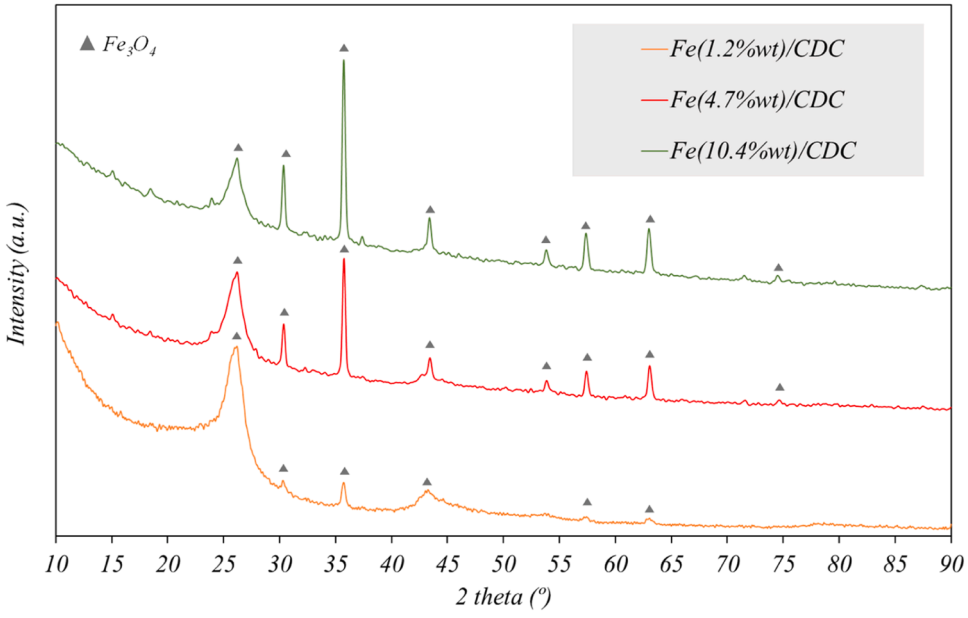

Fig. 6. XRD patterns of Fe(%wt)/CDC catalytic biocarbons after reaction. Conditions: T = 700 ºC, Q_{Total}: 300 mL/min, CO_2/ N_2: 33.3 %/66.7 %.

catalytic biocarbon. The search for the best balance between these two processes is the optimal way to operate. To achieve this, the study of the reaction kinetics of both reactions is of great importance.

3.5. Kinetic modelling of the initial gasification rate, r_{G0}

As previously mentioned, during the reaction, the carbonaceous material undergoes gasification, resulting in a reduction of the sample mass, while iron (Fe) undergoes oxidation. Consequently, the total weight recorded by the thermobalance (W_T) corresponds to the sum of the remaining carbon (W_C) and the weight of the iron oxide formed during the reaction (W_{Ox}), expressed as $W_T = W_C + W_{Ox}$. Since the initial mass of Fe in each sample is known, the maximum amount of oxide formed at the end of the reaction can be estimated under the assumption that the oxide phase corresponds to FeO·Fe₂O₃, as confirmed by the XRD results shown in Fig. 6.

To isolate the effect of Fe deactivation during gasification, the initial gasification rate, r_{G0}, was determined numerically by evaluating the initial slope of the weight vs. time data for all experiments. Under these conditions, at the onset of the reaction, it is assumed that Fe nanoparticles retain their initial catalytic activity. Therefore, for a given Fe(% wt)/CDC sample, the initial gasification rate depends solely on temperature and CO_2 partial pressure. The kinetics of r_{G0} was analysed using both the Power-Law and Langmuir-Hinshelwood models. The Power-Law (P-L) equation is expressed as:

$$r_{G_0} = -\left.\frac{W_C}{dt}\right|_0 = k_p \cdot p_{CO_2}^m \tag{1}$$

Where m is the apparent order of reaction with respect to CO_2, and it should be expected that it does not vary with the temperature. k_p is the kinetic constant, which follows an Arrhenius dependence with the temperature:

$$k_p = k_{p_0} \cdot \exp\left(-\frac{E_p}{RT}\right) \tag{2}$$

k_{p0} is the pre-exponential factor and E_p is the apparent activation energy of the reaction calculated with this model. In the case of the Langmuir-Hinshelwood (L-H) model, the expression used for r_{G0} is:

$$r_{G_0} = -\left.\frac{W_C}{dt}\right|_0 = \frac{k \cdot K_{CO2} \cdot p_{CO_2}}{1 + K_{CO2} \cdot p_{CO_2}} \tag{3}$$

k is the kinetic constant and the term K_{CO2} is the adsorption constant of CO_2. These parameters vary with temperature according to the Arrhenius and Van't Hoff equations respectively:

$$k = k_0 \cdot \exp\left(-\frac{E_a}{RT}\right) \quad ; \quad K_{CO_2} = K_{CO_2,0} \cdot \exp\left(\frac{Q_{CO_2}}{RT}\right) \tag{4}$$

k_0 and $K_{CO2,0}$ are the pre-exponential factors, E_a is the apparent activation energy of the reaction calculated with the LH model and Q_{CO2} is the heat of adsorption of CO_2 on the sample.

Eqs. 1 and 3 can be used to determine the dependence of the reaction rate with respect to the CO_2 concentration for a given temperature. Both equations yield similar fittings since they each contain two parameters: kp and m for the P-L model, and k and K_{CO_2} for the L-H model. However, the physical meaning of these parameters is different, and the dependence with respect to the temperature allows to discriminate with is the most appropriated [24].

Table 3 summarizes the kinetic parameter values obtained using Eqs. (1) and (3) and for each sample, the effect of CO_2 was evaluated for all the temperatures studied.

For the Fe(1.2 %wt)/CDC sample, the values obtained at lower temperatures below 800 °C exhibit anomalies (negative values) due to the effects of the severe diffusional limitations present under these conditions (see Fig. 5).

Table 3
Kinetic parameters of the Power-Law and Langmuir-Hinshelwood models. Influence of the p_{CO2} at the different temperatures studied.

	Temperature (°C)	P-L Model		LH Model	
		k_p	order CO_2 (m)	k	K_{CO2}
Fe(1.2 %wt)/ CDC	*700*	*0.012*	*−2.19*	*0.058*	*−8.894*
	725	*0.008*	*−2.00*	*0.116*	*−67.46*
	750	*0.029*	*−1.56*	*0.205*	*−24.21*
	800	*21.68*	*0.85*	*31.01*	*1.118*
Fe(4.7 %wt)/ CDC	*700*	*7.881*	*0.55*	*6.584*	*5.237*
	725	*10.453*	*0.56*	*8.694*	*5.119*
	750	*12.49*	*0.61*	*11.45*	*3.676*
	800	*21.17*	*0.81*	*26.49*	*1.434*
Fe(10.4 %wt)/ CDC	*700*	*4.833*	*0.31*	*3.709*	*20.61*
	725	*10.48*	*0.58*	*9.087*	*4.392*
	750	*15.55*	*0.73*	*15.23*	*2.419*
	800	*5.587*	*0.85*	*31.87*	*1.240*

However, at 800 °C, the m/m_0 vs. time curves for this sample closely resemble those obtained for the other two samples, Fe(4.7 %wt)/CDC and Fe(10.4 %wt)/CDC.

For the samples with higher Fe content (4.7 %wt and 10.4 %wt), the parameters, k_p (P-L model), and k and K_{CO2} (L-H model) vary with temperature according to Eqs. (2) and (4) respectively.

On the other side, Fig. 7a and 7b presents, for Fe(4.7 %wt)/CDC sample, the effects of reaction temperature and CO_2 concentration on the initial rate of gasification, r_{G0}.

Fig. 7a corresponds to the Arrhenius plot of r_{G0} values, for the three CO_2 concentrations studied. These results indicate that, as expected, the gasification rate increases with p_{CO2}, and more noticeable, that the apparent activation energy increases from 28.4 kJ/mol at 0.083 atm CO_2 to 60.7 kJ/mol at 0.333 atm CO_2, see insert on Fig. 7a.

In addition, Fig. 7b show the effect of the CO_2 concentration at each temperature studied. The results presented in this indicate that the apparent reaction order for CO_2, m_{app}, increases with the temperature from 0.549 at 700 °C to 0.807 at 800 °C, see insert on Fig. 7b.

These results can be explained by considering that the Langmuir-Hinshelwood model can be interpreted as a modified Power-Law model, where the apparent reaction order of CO_2 varies between 0 and 1. In fact, it can be derived that the apparent reaction order of CO_2, $_{mL\text{-}H}$, is given by the following expression [25],[26]:

$$m_{app} = \frac{d\ln(r_{G_0})}{d\ln(p_{CO_2})} = \frac{1}{1 + K_{CO2} \cdot p_{CO_2}} \tag{5}$$

Similarly, to Eq. 5, it can be deduced the expression for the apparent activation energy, as a function of the operating variables [25,26]:

$$E_{app} = -R \cdot T^2 \cdot \frac{d\ln(r_{G_0})}{dT} = E_a - \frac{Q_{CO_2}}{1 + K_{CO2} \cdot p_{CO_2}} = E_a - Q_{CO_2} \cdot m_{app} \tag{6}$$

From the Eqs. (5) and (6), it is evident that both, m_{app} and E_{app}, depend on temperature and CO_2 concentration. Thus, when the adsorption term is significantly greater than 1 (i.e. low temperature and/or high p_{CO2}), the apparent reaction order approaches zero, and the apparent activation energy approaches to that predicted by the LH-model (E_a). Conversely, when the adsorption term is much smaller than 1 (i.e. high temperature or low p_{CO2}), the apparent reaction order approaches 1 and the apparent activation energy vary linearly according to Eq. 6. The obtained values are in the interval with E_a values reported for similar materials [15,27]. Therefore, the values obtained for the apparent orders and activation energy depends on the operating condition used during the gasification tests.

To clarify the combined effect of CO_2 concentration and temperature on the gasification rate, the intrinsic scientific parameters of each model can be directly estimated through non-linear multivariable regression, which provides a statistically more rigorous analysis. This estimation

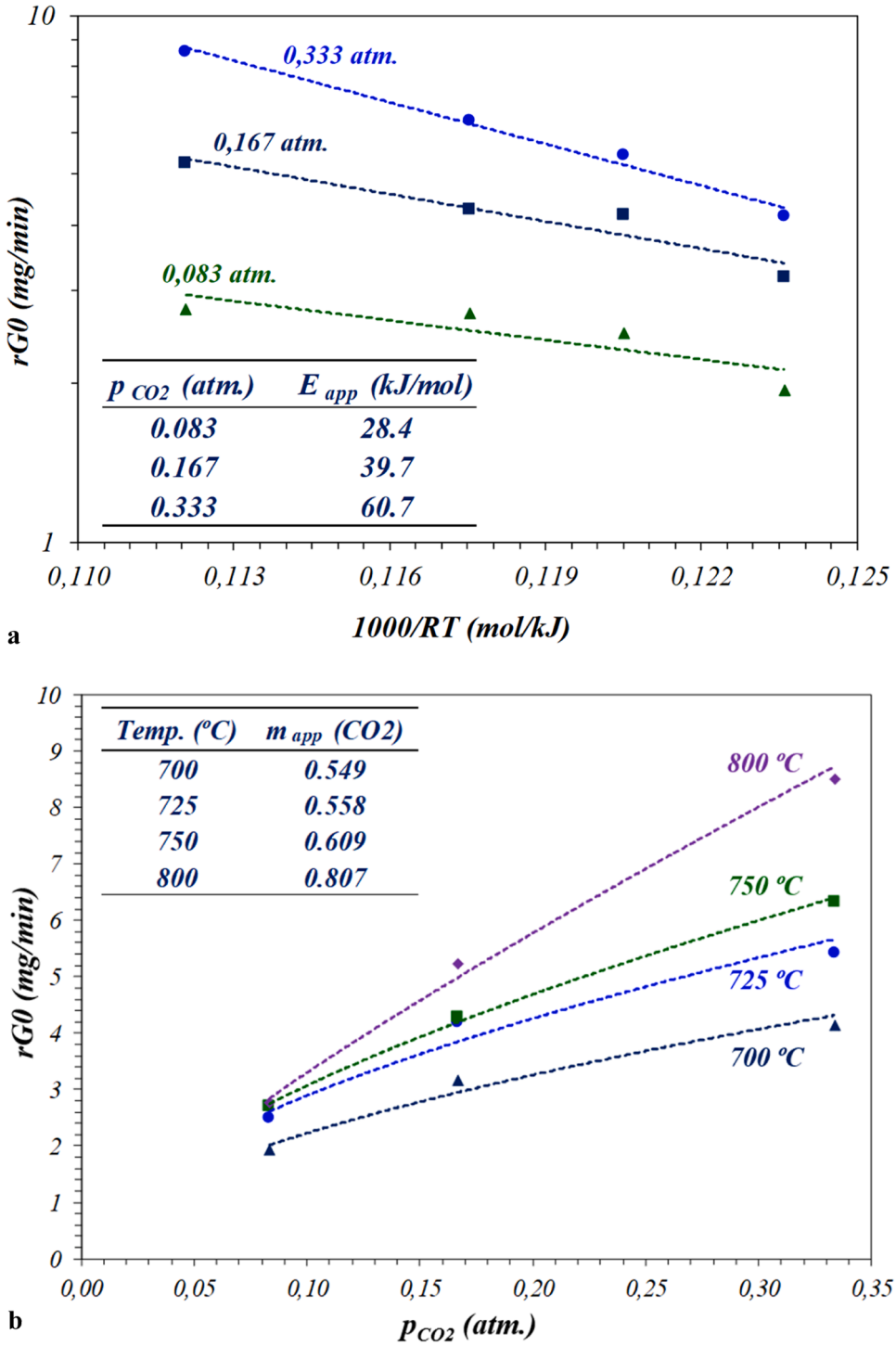

Fig. 7. a). Arrhenius plot of the initial gasification rate for the Fe(4.7 %)/CDC sample. Influence of the partial pressure of CO_2 on the apparent activation energy; b). Effect of CO_2 concentration on the initial gasification rate. Influence of reaction temperature or the apparent kinetic order.

process employs the Model Selection Criterion (*MSC*) as the objective function [28], defined as:

$$MSC = ln\left(\frac{1}{1-R^2}\right) - \frac{2 \cdot n}{n-p} \tag{7}$$

Where n is the number of experimental points and p the number of parameters of each model. The value or the coefficient of determination, R^2, is approximated as:

$$R^2 = \frac{SST - SSR}{SST} \tag{8}$$

Where the terms *SST*, *SSR* are the sum of squared totals and squared residuals, respectively:

$$SST = \sum_n \left(r_{G_0,\exp} - \overline{r_{G_0,exp}}\right)^2 \quad ; \quad SSR = \sum_n \left(r_{G_0,\exp} - r_{G_0,cal}\right)^2 \tag{9}$$

The term $\overline{r_{G_0,exp}}$ is the average value of the experimental data:

$$\overline{r_{G_0,exp}} = \frac{\sum_n r_{G_0,\exp}}{n} \quad (10)$$

The Power Law model has three intrinsic parameters (k_{p0}, E_p, and m), while the Langmuir-Hinshelwood model includes four (k_0, E_a, $K_{CO2,0}$ and Q_{CO2}). As a result, the L-H model is expected to provide a better fit to the data, reflected in a lower sum of squared residuals (SSR). However, the Model Selection Criterion (*MSC*) enables discrimination between models with different numbers of parameters, as it not only considers the coefficient of determination (R^2) but also penalizes models with a higher number of parameters. Consequently, the model with the highest *MSC* value is selected as the most appropriate. Regardless, all estimated parameter values must be physically meaningful and satisfy all kinetic and thermodynamic constraints [29].

In Table 4 are summarized the values of the intrinsic kinetic parameters obtained with both models for the Fe(4.7 %wt)/CDC sample. In the table are also include the estimation of the standard error of each parameter and the confidence interval at 95 % of confidence.

As observed, all values are statistically significant, as no negative values are obtained for the lower limits, indicating the high quality of both fittings. The coefficients of determination (R^2) and the Model Selection Criterion (*MSC*) values are 0.9649 and 2.6825 for the P-L model, and 0.9933 and 4.0122 for the L-H model, respectively. These results confirm that the Langmuir-Hinshelwood model is the more appropriate choice for describing the initial gasification rate.

The intrinsic parameter values presented in Table 4 provide an explanation for the results previously shown in Table 3 and Fig. 6 and 7. Thus, as can be seen in Table 4, the value of the activation energy, E_a, calculated for the L-H model, 120.3 kJ/mol, is much higher that the corresponding value of the P-L model, E_p = 49.1 kJ/mol, indicating the in fact the P-L model is an average approximation of the L-W, and the kinetic parameter are less consistent. Furthermore, these findings can be used to model the curves in Fig. 5 and, ultimately, the overall gasification process.

4. Conclusions

The incorporation of iron into catalytic biocarbons significantly influences their physicochemical and catalytic properties. As the iron content increases, the textural properties of the materials are modified, leading to a reduction in surface area and pore volume, as well as an increase in pore size. This structural evolution enhances CO_2 diffusion, thereby improving the reactivity of the biocarbon in the gasification process. Additionally, higher Fe loading results in the formation of larger Fe particles within the catalytic biocarbon. These factors, along with the operating conditions, collectively impact the gasification performance.

Table 4
Intrinsic kinetic parameters of the Power-Law and Langmuir-Hinshelwood models for the Fe(4.7 %wt)/CDC sample.

Parameter P-L model	*Value*	*Standard Error*	*Confidence Interval (95 %)*	*Lower Limit (95 %)*	*Upper Limit (95 %)*
k_{p0} (mg/min.atm^m)	12.782	0.99	2.244	10.538	15.027
E_p (kJ/mol)	49.1	5.65	12.8	36.3	61.9
m (CO_2) (-)	0.637	0.051	0.116	0.521	0.753
Parameter L-H model	***Value***	***Standard Error***	***Confidence Interval (95 %)***	***Lower Limit (95 %)***	***Upper Limit (95 %)***
k_0 (mg/min)	12.420	0.805	1.857	10.562	14.277
E_a (kJ/mol)	120.3	12.9	29.9	90.5	150.2
$K_{CO2,0}$ (atm^{-1})	3.265	0.365	0.842	2.423	4.107
Q_{CO2} (kJ/mol)	125.2	20.8	47.9	77.3	173.0

The presence of Fe in the biocarbon notably lowers the gasification temperature, demonstrating the catalytic effectiveness of iron in the process. The gasification rate increases with temperature, particularly between 750 °C and 800 °C, where a higher degree of biocarbon conversion is observed. At lower temperatures (700 °C), an induction period is evident, slowing down the reaction, especially in materials with lower iron content, where the microporosity of the carbonaceous support is more pronounced. Furthermore, CO_2 concentration has a significant impact on gasification, particularly at lower temperatures, where higher CO_2 levels inhibit the process due to the oxidation of metallic species. However, at elevated temperatures (800 °C), this inhibitory effect is less pronounced, allowing for a more efficient gasification process within a shorter time frame.

Characterization by XRD, TGA, Raman, TEM, and N_2 adsorption revealed that the initial Fe loading in cellulose not only determines the final carbon content in each Fe(%wt)/CDC sample but also plays a crucial role in shaping the textural and structural properties of the resulting carbonaceous materials, as well as the Fe nanoparticle size distribution. Specifically, increasing the Fe content leads to a decrease in surface area, a reduction in microporosity, an increase in pore diameter, and the formation of larger Fe nanoparticles. However, during gasification, Fe nanoparticles are oxidized by CO_2, resulting in a decline in catalytic activity and ultimately limiting the complete gasification of the carbonaceous material. These competing effects account for the varying behaviours observed in the Fe(%wt)/CDC samples studied.

Analysis of the initial gasification rates indicated that both the apparent reaction order with respect to CO_2 and the activation energy increased with reaction temperature and CO_2 partial pressure (pCO_2), respectively. These results were successfully interpreted using a Langmuir-Hinshelwood model, which accounts for the influence of CO_2 adsorption on the observed reaction rate.

Overall, Fe(%wt)/CDC catalytic biocarbons show great potential for biomass gasification processes. Optimizing temperature and CO_2 concentration conditions can enhance process efficiency and reduce energy consumption, making these materials promising candidates for sustainable carbon conversion technologies.

Funding sources

Grants PID2020-113809RB-C31 and PID2023-147861OB-C21 funded by MICIU/AEI/10.13039/501100011033. D. Chaos-Hernández thanks the MICINN/AEI for funding from the Pre-doctoral contract. Ref.: PRE2021-09794.

CRediT authorship contribution statement

Eva Romeo: Methodology, Formal analysis, Data curation, Conceptualization. **Antonio Monzon:** Project administration, Methodology, Formal analysis, Conceptualization. **David Chaos-Hernandez:** Methodology, Investigation, Data curation. **Nieves Latorre:** Supervision, Methodology, Conceptualization. **Pilar Tarifa:** Methodology, Investigation, Data curation.

Declaration of Competing Interest

The authors of the manuscript entitled "**Influence of operating conditions on the kinetics of Iron-catalysed gasification of biocarbons with CO2**", by D. Chaos-Hernandez et al., submitted for consideration in the Special Issue "Iberoamerican Catalysis Congress - Innovating for a changing world", declare that this work:

- has not been published previously
- the article is not under consideration for publication elsewhere
- the article's publication is approved by all authors and tacitly or explicitly by the responsible authorities where the work was carried out.

- if accepted, the article will not be published elsewhere in the same form, in English or in any other language, including electronically, without the written consent of the copyright-holder.

Acknowledgements

The authors would like to thank the SAI, University of Zaragoza, and the Government of Aragon for their collaboration, Ref. of the research group T22_23R.

Appendix A. Supporting information

Supplementary data associated with this article can be found in the online version at doi:10.1016/j.cattod.2025.115289.

Data availability

Data will be made available on request.

References

[1] R. Roncancio, J.P. Gore, CO2 char gasification: a systematic review from 2014 to 2020, Energy Convers. Manag.: X 10 (2021), https://doi.org/10.1016/j.ecmx.2020.100060.
[2] P. Lahijani, Z.A. Zainal, M. Mohammadi, A.R. Mohamed, Conversion of the Greenhouse gas CO2 to the fUel Gas CO via the Boudouard Reaction: a Review, Elsevier Ltd. (2015), https://doi.org/10.1016/j.rser.2014.08.034.
[3] A. Khajeh, S. Masoumi, L. Wang, A. Shahbazi, Effects of various carbon-supported iron catalysts on tar removal efficiency and syngas yield during catalytic biomass gasification, J. Environ. Chem. Eng. 11 (5) (2023), https://doi.org/10.1016/j.jece.2023.110884.
[4] M. Kumar, R.C. Gupta, Industrial uses of wood char, Energy Sources 20 (7) (1998) 575–589, https://doi.org/10.1080/00908319808970079.
[5] Y. Wang, R. Yoshiie, Y. Ueki, I. Naruse, Effect of temperature on behavior and mechanism of biochar gasification in the mixed CO2 and H2O atmosphere, J. Energy Inst. 108 (2023), https://doi.org/10.1016/j.joei.2023.101238.
[6] F. Zhang, D. Xu, Y. Wang, M.D. Argyle, M. Fan, CO2 gasification of Powder River Basin coal catalyzed by a cost-effective and environmentally friendly iron catalyst, Appl. Energy 145 (2015) 295–305, https://doi.org/10.1016/j.apenergy.2015.01.098.
[7] Y. Jiang, H. Yan, Q. Guo, F. Wang, J. Wang, Multiple synergistic effects exerted by coexisting sodium and iron on catalytic steam gasification of coal char, Fuel Process. Technol. 191 (2019) 1–10, https://doi.org/10.1016/j.fuproc.2019.03.017.
[8] B. Xu, et al., Kinetics and mechanism of CO2 gasification of coal catalyzed by Na2CO3, FeCO3 and Na2CO3–FeCO3, J. Energy Inst. 93 (3) (2020) 922–933, https://doi.org/10.1016/j.joei.2019.08.004.
[9] Y. Ohtsuka, Y. Tamai, A. Tomita, Iron-catalyzed gasification of Brown coal at low temperatures, (Online) (1987) (https://pubs.acs.org/sharingguidelines).
[10] X. Qi, X. Guo, L. Xue, C. Zheng, Effect of iron on Shenfu coal char structure and its influence on gasification reactivity, J. Anal. Appl. Pyrolysis 110 (1) (2014) 401–407, https://doi.org/10.1016/j.jaap.2014.10.011.
[11] F. Cazaña, et al., Synthesis of Pd-Al/biomorphic carbon catalysts using cellulose as carbon precursor, Catal. Today 301 (May 2017) (2018) 226–238, https://doi.org/10.1016/j.cattod.2017.05.026.
[12] L.E.A. Harold P. Klug, X-Ray Diffraction Procedures: For Polycrystalline and Amorphous Materials, second, ilustra ed., 1974.
[13] Y. Xie, et al., Study on CO2 gasification of biochar in molten salts: reactivity and structure evolution, Fuel 254 (2019), https://doi.org/10.1016/j.fuel.2019.06.022.
[14] A. Gil, J. Pallarés, I. Arauzo, C. Cortés, Pyrolysis and CO2 gasification of barley straw: Effect of particle size distribution and chemical composition, Powder Technol. 424 (2023), https://doi.org/10.1016/j.powtec.2023.118539.
[15] P. Lahijani, Z.A. Zainal, A.R. Mohamed, Catalytic effect of iron species on CO 2 gasification reactivity of oil palm shell char, Thermochim. Acta 546 (2012) 24–31, https://doi.org/10.1016/j.tca.2012.07.023.
[16] W. Liang, et al., Influence mechanism and kinetic analysis of co-gasification of biomass char and semi-coke, Renew. Energy 163 (2021) 331–341, https://doi.org/10.1016/j.renene.2020.08.142.
[17] M.T.S. Lowell, Joan E. Shields, Martin A. Thomas, Characterization of Porous Solids and Powders: Surface Area, Pore Size and Density, first ed., Springer Dordrecht, 2004. doi: https://doi.org/10.1007/978-1-4020-2303-3.
[18] X. Zeng, K. Kahara, Y. Ueki, R. Yoshiie, G. Xu, I. Naruse, Characteristics of biomass devolatilization and in situ char gasification tested by the non-isothermal method, Energy Fuels 33 (10) (2019) 9805–9817, https://doi.org/10.1021/acs.energyfuels.9b00672.
[19] G. De Micco, A. Nasjleti, A.E. Bohé, Kinetics of the gasification of a Rio Turbio coal under different pyrolysis temperatures, Fuel 95 (2012) 537–543, https://doi.org/10.1016/j.fuel.2011.12.057.
[20] M.A. Kibria, P. Sripada, S. Bhattacharya, Steady state kinetic model for entrained flow CO2 gasification of biomass at high temperature, Energy 196 (2020), https://doi.org/10.1016/j.energy.2020.117073.
[21] M. Ma, et al., Development of multiple alkali metals doped La-Ni based perovskites for CO2 gasification of biochar to produce CO rich syngas, J. Energy Inst. 114 (2024), https://doi.org/10.1016/j.joei.2024.101637.
[22] D. Chaos-Hernández, N. Latorre, P. Tarifa, E. Romeo, A. Monzón. Modelling the CO_2 Gasification of Iron-Modified Biomass Carbons: a Kinetic Approach, In preparation, 2025.
[23] T. Nordgreen, T. Liliedahl, K. Sjöström, Metallic iron as a tar breakdown catalyst related to atmospheric, fluidised bed gasification of biomass, Fuel 85 (5–6) (2006) 689–694, https://doi.org/10.1016/j.fuel.2005.08.026.
[24] M. Boudart and G. Djega-Mariadassou, Kinetics of Heterogeneous Catalytic Reactions, Princeton University Press, 1984. doi: 10.1515/9781400853335.
[25] I. Chorkendorff and J.W. Niemantsverdriet, Concepts of Modern Catalysis and Kinetics, Wiley, 2003. doi: 10.1002/3527602658.
[26] S. Armenise, E. García-Bordejé, J.L. Valverde, E. Romeo, A. Monzón, A Langmuir–Hinshelwood approach to the kinetic modelling of catalytic ammonia decomposition in an integral reactor, Phys. Chem. Chem. Phys. 15 (29) (2013) 12104, https://doi.org/10.1039/c3cp50715g.
[27] Y.S. Baath, P.A. Nikrityuk, R. Gupta, Experimental and numerical verifications of biochar gasification kinetics using TGA, Renew. Energy 185 (2022) 717–733, https://doi.org/10.1016/j.renene.2021.12.091.
[28] S.L. Sclove, Application of model-selection criteria to some problems in multivariate analysis, Psychometrika 52 (3) (1987) 333–343, https://doi.org/10.1007/BF02294360.
[29] M.A. Vannice, Kinetics of Catalytic Reactions, Springer, New York (USA), 2005, https://doi.org/10.1007/b136380.